Available online at www.ijournalse.org

Emerging Science Journal

(ISSN: 2610-9182)

Vol. 9, No. 6, December, 2025

Small Dual Polarized UWB Antenna and Its Array Analysis for 5G/6G Applications

Amir Reza Dastkhosh [1*], Abolfazl Mehbodniya [2], Julian Webber [2], Mehdi Naseh [3], M. Dadras Jedi [1], Fujiang Lin [1]

[1] *University of Science and Technology of China, Hefei, China.*

[2] *Department of Electronics and Communication Engineering, Kuwait College of Science and Technology (KCST), Kuwait City 13133, Kuwait.*

[3] *University of Mons, Mons, Belgium.*

Abstract

In this work, a novel low-profile tunable ultra-wideband (UWB) K/Ka-band (14–40 GHz) dual circularly polarized magneto-electric antenna element has been designed, analyzed, and validated through circuit modeling, simulations, fabrication, and experimental testing for application in 5G/6G phased-array antennas. The antenna has compact dimensions of $0.5\lambda_0 \times 0.5\lambda_0 \times 0.06\lambda_0/0.09\lambda_0$, which can be further reduced to $0.25\lambda_0 \times 0.25\lambda_0 \times 0.05\lambda_0$ when metal–insulator–metal (MIM) and/or gap capacitors are employed. The proposed antenna exhibits a high gain of 9 dB, a wide scanning angle of ±75°, and an efficiency exceeding 85% across the entire operating frequency band. In addition, it demonstrates high isolation between ports and between co-polarized and cross-polarized radiation patterns, reaching 25 dB. The resonant frequency of the antenna is tunable, with a variation of up to 97% over the K/Ka-band frequency range. This tuning capability is achieved using MIM capacitors connected to the vias of the circular patch and/or gap capacitors, which collectively function as split-ring resonators (SRRs). Fabrication and experimental testing of the antenna confirm good agreement with the simulated results. The antenna is easily fabricated using glass substrates and standard epoxy/glass processes with only two layers, making it highly suitable for antenna-in-package applications based on glass technology. Since the antenna element is specifically designed for phased-array applications, array configurations were also investigated. Analysis of 512-element arrays shows that the Sunflower layout provides enhanced gain and overall performance while utilizing more than 50% fewer antenna elements compared to a conventional rectangular array.

Keywords:

Antenna-in-Package;
Dual Circularly-Polarized Antenna;
Magneto-Electric Dipole (MED);
Phased Array Antennas;
SRR;
Ultrawideband (UWB).

Article History:

Received:	09	April	2025
Revised:	11	November	2025
Accepted:	14	November	2025
Published:	01	December	2025

1- Introduction

Innovative wireless technologies have progressed in response to the constraints of earlier wireless communication systems, characterized by low data rates and connection density [1-4]. Academia and industry must now prioritize the advancement of next-generation wireless technology. Path loss and the adjustment of transmitter and receiver antenna beam angles for mobile entities, such as cars, while minimizing latency, present significant communication challenges. Millimeter wave (mmWave) phased array antennas in satellite mobile communications can satisfy the increasing demand for enhanced data rates and reduced latency. Low earth orbit (LEO) and geostationary orbit (GEO) satellites, together with space Internet, are becoming significant, particularly as sixth-generation (6G) systems seek to integrate satellite internet with 5G wireless terrestrial stations [5-9]. Effective millimeter-wavelength satellite communications necessitate the enhancement or replacement of existing systems and a transition from the centimeter band spectrum [10-16].

* **CONTACT**: amirreza@mail.ustc.edu.cn

DOI: http://dx.doi.org/10.28991/ESJ-2025-09-06-04

Glass substrates are increasingly favored in packaging due to their thermal stability and electrical insulating properties. Glass technologies are appealing for high-volume, high-performance radio frequency (RF) applications because of their minimal dielectric losses, smooth surfaces, and dimensional stability [16-19]. Glass substrates are optimal for photonics, display technologies, and sensors, since their thermal and chemical stability, together with optical clarity, are essential for superior optical and mechanical performance. Moreover, glass-based antennas are cost-effective, adaptable in architectural design, and suitable with vehicles and ships. Transparent antennas integrated with solar cells for satellite communication provide an innovative approach to enhance energy harvesting, guarantee reliable satellite-to-ground communications, and save payload weight.

Platform independence is essential for antennas on mobile platforms such as automobiles and vessels to function effectively in various conditions. Compact modules incorporating transceivers and antennas or subarrays are enhanced by the antenna-in-package (AiP) configuration. RF systems require AiP technology to enhance functional density, efficiency, and compactness while reducing costs. This technology reduces transmission line losses and structural complexity and will revolutionize 5G and next mmWave antenna architecture. Low loss glass-based AiP can be constructed utilizing hybrid substrate technology or flip chip ball grid array (FCBGA) technologies to address heat dissipation, integration, and chip interconnections, ensuring highly reliable systems [20-22]. FCBGA technology enhances RF performance and system-level integration in AiP packages, rendering them suitable for 5G/6G applications, IoT devices, and other high-frequency communication systems. The AiP approach vertically arranges RF components like as filters, power amplifiers, and antennas in three dimensions, thereby optimizing space and minimizing system size [23, 24].

The following are the design goals for the Ka-band phased array antenna using AiP modules/elements: a) calculating the gain of the active phased array antenna based on the characteristics of the antenna elements, such as gain, efficiency, transmitter power, and link budget analysis [12-15]; b) designing a phased array antenna element using Glass technology specifications. The array must ensure effective isolation of the antenna elements. The design specifications are as follows: frequency: Ka; polarization: dual linear/circular (to reduce loss); gain: greater than 2dB; broad scanning angles: $|\theta|$ greater than 60°; isolation: greater than 20dB (to be compatible with any array layout).

The design of the antenna element may encompass a wide variety of options, including patch antennas, as referenced in the literature [25-43]. One of the best antenna candidates that can cover the mentioned specifications and be implemented on Glass substrates are MED antennas. Nonetheless, previously designed MED antennas suffer from some problems including: preparing narrow bandwidth [26, 27], are suitable for low frequencies [28-30], are bulky and spacious with large footprints and needing complex fabrication technologies and exhibit poor cross-polarization suppression [31-37]. Although previous studies have demonstrated the effective design of these antennas, as noted by Chaloun et al. [24], and have occasionally incorporated filtering capabilities as seen in Tian .et al [38], or have achieved compactness as indicated in Yang .et al [39], or utilized differential feeding as described by Yang et al. [40], many of these designs have been implemented on thick substrates. Furthermore, they often necessitate costly advanced fabrication techniques such as high-density interconnector (HDI) packaging or fan-out wafer-level packaging (FOWLP), or they may feature multilayered complex structures, or lack dual polarization [41, 42].

The design of the MED antenna is presented here to satisfy the specifications and limitations for AiP glass-based packaging, including both electrical and geometric requirements. A small, low-profile antenna exhibiting minimal volume and broadside radiation, comparable in size to an integrated circuits (IC) with dual feeding, is suitable for AiP glass-based packaging. Theoretical analysis and calculations for the design of the proposed antenna are initially provided. Subsequently, the structure undergoes optimization and simulation. The finalized antenna specifications are confirmed through fabrication and measurement processes.

This paper introduces an innovative, low-profile, easily fabricated, and cost-effective dual-polarized MED antenna, specifically designed and simulated for satellite mobile communication systems (SATCOM). The antenna utilizes both Glass and traditional substrates, and its circuit model is presented. Glass substrates (ε_r ~2.5–10) enable thinner profiles and some of them low loss tangent as well but require trade-offs in efficiency and frequency bandwidth vs. Rogers materials [17, 24, 43]. The design methodology can be easily accommodated with this range with minor dimensional adjustments. The final antenna configuration is validated through simulations conducted using CST Studio Suite, as well as through fabrication and testing based on available substrates and fabrication technology of multilayered PCBs. The proposed antenna element is characterized by a more compact and thinner design, offering a broader scanning angle and wider frequency bandwidth in comparison to prior designs, while also supporting various forms of polarization. Its structure is well-suited for AiP applications based on Glass technology comprising only two layers. Additionally, array analyses of the designed antenna demonstrate that the performance of the Sunflower array exceeds that of the rectangular one.

2- Proposed Antenna Design

This section elucidates the design and analysis of the proposed antenna. The proposed antenna configuration is based on MED antennas (MEDAs). Consequently, a conventional MEDA can function as a benchmark for analysis and design. In fact, within the realm of patch antennas, MEDAs are designed using a planar half-wavelength dipole and a shorted

quarter-wavelength patch antenna, functioning as electric and magnetic dipoles, respectively. MEDA, functioning as a complementary antenna or Huygens' source, is distinguished by its elevated gain and extensive bandwidth, resulting from the concurrent excitation of both electric and magnetic dipoles with similar signal amplitude and phase. The radiation released by the shorted quarter-wave patch antenna primarily emanates from its open end, functioning as a magnetic current source.

The structure and modelling of the proposed antenna with its magnetic dipoles (MDs) and folded electric dipoles (FEDs) are illustrated in Figure 1. To prevent polarization loss, the proposed antenna must also support circular polarization. To achieve circular polarization and broader scanning angles, a circular patch antenna is initially designed. Therefore, the antenna can be analyzed as a cavity, and its effective radius can be determined using the following calculation [25]:

$$r_{eff} = r\sqrt{1 + \frac{2h}{\pi r \varepsilon_r}\left(ln\frac{\pi r}{2h} + 1.77\right)} \quad (1)$$

where; h is the thickness of the substrate, ε_r is the electrical permittivity of the dielectric, and r and r_{eff} are the values of actual radius and effective radius of a circular patch antenna.

Similar to a circular patch antenna or, more specifically, a conventional MEDA, the radiation patterns of the electric dipole exhibit a "inverted-8" configuration in the E-plane and an omnidirectional pattern in the H-plane, whereas the magnetic dipole displays a "inverted-8" configuration in the H-plane and an omnidirectional pattern in the E-plane [25, 44, 45]. The presence of a ground plane facilitates reflection, thereby enhancing the antenna's gain and minimizing back-lobe radiation.

The proposed MEDA can be effectively analyzed within the framework of Hertzian dipole antennas, as the electric dipole component is represented as a Hertzian dipole (short current element), while the magnetic dipole component is depicted as a small loop antenna, reflecting the duality with the Hertzian dipole. An electric Hertzian dipole of length dy, oriented along the y-axis, can be represented as an electric current $I = H_x dx$, while a magnetic Hertzian dipole of length dx, aligned along the x-axis, corresponds to a magnetic current, $I_m = E_y dy$. Consequently, the antenna has cosine normalized radiation patterns in planes of any φ. Hence, the radiation characteristic of the complementary antenna confirms that this concept can be applied for developing unidirectional antennas. The characteristic of the complementary antenna supports the feasibility of developing unidirectional antennas based on this concept. Hence, the electric field in the far-field zone can be expressed as [45]:

$$\vec{E} = -j\frac{\mathrm{Idy}}{2\lambda r}\eta\left(\vec{e}_\theta \cos\theta \, sin\varphi + \vec{e}_\phi cos\varphi\right)e^{-jkr} \quad (2)$$

While a magnetic Hertzian dipole with a length of dx, placed along the x-axis, is equivalent to a magnetic current, $I_m = E_y dy$. Hence, the electric field in the far-field zone can be expressed as:

$$\vec{E} = j\frac{I_m \mathrm{dx}}{2\lambda r}\left(\vec{e}_\theta \sin\varphi + \vec{e}_\phi cos\theta cos\varphi\right)e^{-jkr} \quad (3)$$

The far-field electric field is obtained by adding the above equations:

$$\vec{E} = j\frac{E_y \mathrm{dxdy}}{2\lambda r}[\vec{e}_\theta sin\varphi(1 + cos\theta) + \vec{e}_\phi cos\varphi(1 + cos\theta)]e^{-jkr} \quad (4)$$

Consequently, the normalized radiation patterns in planes of any φ are the same and can be expressed as:

$$F(\theta) = \frac{\sqrt{sin^2\varphi(1+\cos\theta)^2 + cos^2\varphi(1+\cos\theta)^2}}{2} = \frac{(1+\cos\theta)}{2} \quad (5)$$

when θ = 180°, F(θ) = 0, indicating that there is no back radiation. Hence, the radiation characteristic of the complementary antenna confirms that this concept can be applied for developing unidirectional antennas.

The impedance characteristic of the designed antenna is investigated by geometry and the equivalent circuit of the proposed antenna shown in Figure 1. The patch antenna has a fundamental resonant mode which can be represented by a parallel resonant circuit (resistance R_m, capacitance C_m, and inductance L_m), whereas the electric dipole has a fundamental mode which can be represented by a series resonant circuit (resistance R_d, capacitance C_d, and inductance L_d). The L-probe feed is modelled by an inductor L_f and capacitor C_f. $C_{MG} = C_{MIM}s + C_{GAP}s$, is the total capacitance including parallel capacitors with VIAs and/or grounded inductors and gap capacitances. It can tune or decrease the resonant frequency of the proposed antenna. When the two circuits are connected in parallel, the input admittance is:

$$Y_{in} = j\omega C_{MG} + \left[\frac{1}{R_d + j\left(\omega L_d - \frac{1}{\omega C_d}\right)}\right] + \left[\frac{1}{R_m} + j\left(\omega C_m - \frac{1}{\omega L_m}\right)\right] \quad (6)$$

It can be observed that the imaginary part of the input admittance of the complementary antenna can be canceled out if:

$$C_d L_d = C_m L_m,\ R^2 = L_d / C_m \tag{7}$$

In order for both equations to be concurrently satisfied, it is essential that the resonant frequencies of the electric dipole and the patch antenna are equal. Additionally, the input resistance of the electric dipole must be adjusted to a value that is proportional to the reactive components of both the dipole and the patch antenna. The folded L-shaped probe/patch greatly influences the impedance matching of the antenna. The height of the magnetic dipole, composed of a shorted quarter-wave patch antenna, is mostly determined by the magnetic dipole itself.

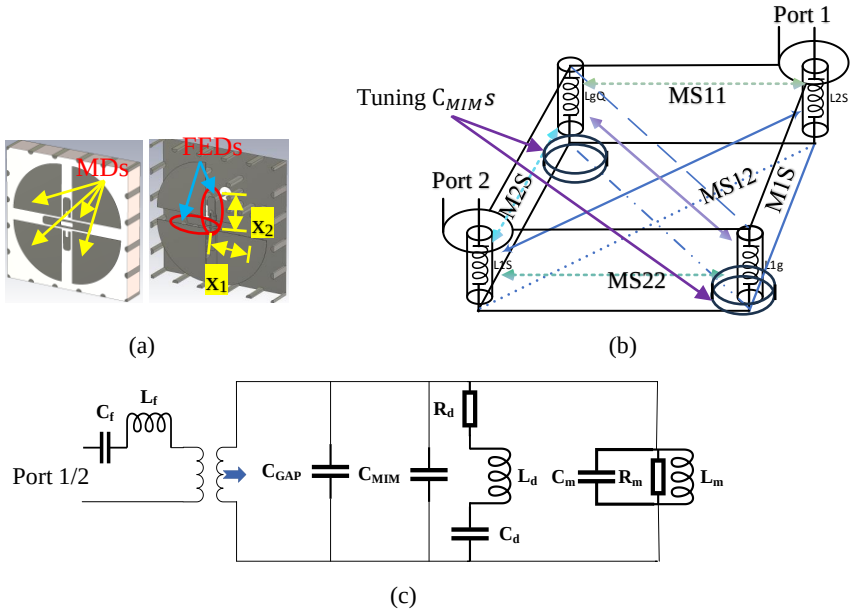

Figure 1. Proposed antenna modelling; a) antenna structure, b) modelling VIAs of the proposed antenna [33] and tuning capacitors, c) proposed equivalent circuit model

To provide a significant degree of isolation, VIAs and two orthogonal, folded cross-feeding lines are designed with differing elevations. The terminals of these lines are linked to a SMA connection to enable the antenna's excitation. Moreover, the tapered design of the Γ-shaped feeding lines introduces adjustable parameters and enhances the optimization of impedance matching. The VIAs enable the ingress of current and electromagnetic fields into the antenna. In our design, if we suppose r = 0.25λ_0, h = 0.05λ_0, $\varepsilon_r = 3.5$, so we have: h/r = 0.2 and $r_{eff} \approx 1.07r$. The lowest resonant frequency for the geometry with the value of r = 2.2mm will be: $(f_r)_{110}^{TE^z} \approx 20GHz$. However, due to the supplementary capacitors and the configuration of the proposed antenna, which will be examined in the subsequent paragraphs, the antenna is capable of resonating at lower frequencies.

The single port excitation, akin to the differential-fed mechanism excites the TE_{11} mode (fundamental mode) in the cavity/antenna due to the placement of feeding points along the central axis of the structure, generating surface currents or electric fields along these lines [19]. The inductance values generated solely by VIAs and the coupling effects can be computed using [46]:

$$L = \frac{\mu_0 h}{2\pi}\left[\ln\left(\frac{x_1+x_2}{4(a)}\right) - 0.75\right] \tag{8}$$

$$M = \frac{\mu d}{2\pi}\left[\ln\left(\frac{x_1+x_2}{4(s_{1k}+a)}\right) - 0.75\right] \tag{9}$$

where, h is the thickness of the substrate, x_i (Figure 1) are the geometrical dimensions of a specific area, s_{1k} are the distances separating the signal VIAs and grounded VIAs, d is the distance among grounded VIAs and a is the radius of the VIAs. As can be seen from the circuit model and the formulas, the mutual couplings among VIAs and ports act as impedance transformers. Also, the MIM capacitors and the capacitances that are created by metal gaps can be calculated by [45-47]:

$$C_{MIM} = \frac{\varepsilon_r S}{4\pi k d_m};\ C_{GAP} = \frac{\pi \varepsilon_r w}{ln(g/t)} \tag{10}$$

where; S is the overlapping area of a MIM capacitor, d_m is the thickness of the dielectric, k is the electrostatic constant, l is the total length of each resonator, w is the width of the metallic sheet (here the average widths of the quarter-patches), g is the gap distance of the Gap capacitor and t is the thickness of metal strip. Also, line inductors (L_1) and line inductors including VIAs (L_2) are calculated by:

$$L_1 = 2l\left[ln\frac{l}{w+t} + 0.5 + \frac{w+t}{3l}\right] \tag{11}$$

$$L_2 = \frac{\mu_0}{2\pi}\left[h\, ln\frac{h+\sqrt{h^2+a^2}}{a} - \sqrt{h^2+a^2} + \frac{h}{4} + a\right] \quad (12)$$

MIM capacitors are primarily created between middle and top layer (by radiating patched and feed lines). However, the gap capacitors are primarily located in the feeding lines. MIM capacitors in comparison with interdigital ones prepare larger values and have more compact sizes too. The total inductance and capacitance will be a combination of the series and parallel ones [48]:

$$f_r = \frac{1}{2\pi\sqrt{L_t C_t}} \quad (13)$$

For example, for the proposed antenna and h = 1mm, r ≈ 0.15 mm; $L_t \approx L \approx L_2/20 \approx 0.75\text{nH}, C_t \approx C_{MG} \approx 0.3\text{pF}$: (f ≈ 30GHz). By tuning the values of (MIM/gap) capacitors and VIAs as inductors, the resonant frequency reaches to 20GHz or even less (14GHz). Briefly, the design procedure of the proposed antenna can be outlined as follows:

a) Calculating the size of the conventional circular patch antenna,

b) Designing matched Γ-shaped feeding mechanism,

c) Obtaining circuit model, tuning of parameters/dimensions using CST Studio Suite to attain a high-performance antenna,

d) Incorporate MIM capacitors in the antenna structure to make the antenna more compact,

e) Develop a dual-port antenna and implement final improvements, optimizations and adjustments.

Figure 2 illustrates a flowchart summarizing steps (a)–(e).

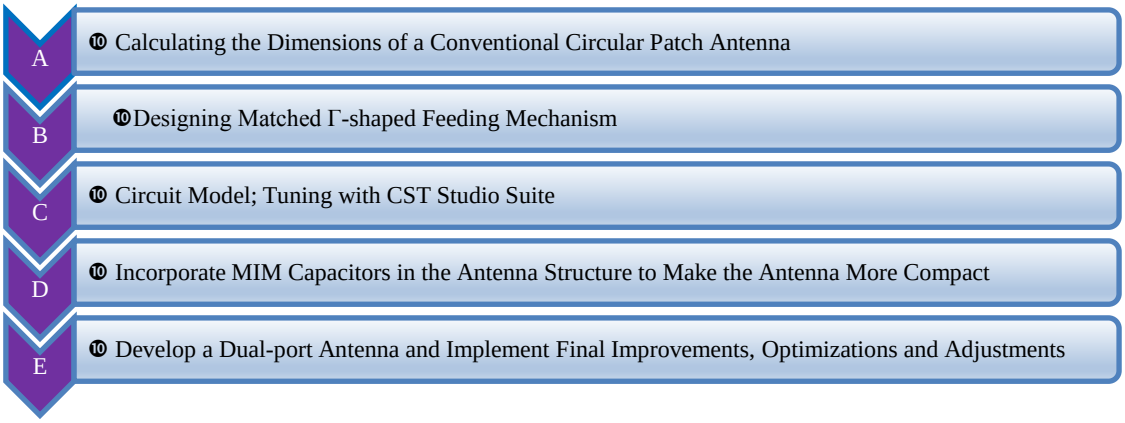

Figure 2. The flowchart of the design

A. Active Impedance and Scan Blindness

Surface waves and mutual coupling may result in scan blindness; yet, these issues can be mitigated with designing cavity-based low-profile structures, optimal shielding, and grounded VIAs [49, 50]. Hence, it is recommended to utilize a thin substrate with a lower dielectric constant. For calculating the active element pattern, all feed voltages are set to zero except for the nth generator, which is set to unity:

$$R(\theta,\varphi) = \frac{Z_{in}(\theta,\varphi) - Z_{in}(0,0)}{Z_{in}(\theta,\varphi) - Z_{in}^{*}(0,0)} \quad (14)$$

where; R is reflection coefficient in feed line connected with microstrip dipole, θ and φ are the phased array scan angles. If R ($\theta_{bl}, \varphi_{bl}$) = 1, then θ_{bl} and φ_{bl} are the microstrip phased array blindness angles.

The Floquet analysis method is employed to examine and simulate the antenna element inside the array. This analysis describes fields interacting with periodic structures through Floquet's (or Bloch's) theorem, which states that fields within a periodic structure are quasi-periodic, indicating they are periodic with respect to a specific phase difference and attenuation [51]. To avoid the appearance of grating lobes, the distances between antenna elements must: $d \leq \lambda_0/(1+\sin(\theta))$. In large (periodic) arrays, the goal is to solve partial diff erential equations with periodic boundaries conditions, for instance by finite element method (FEM), the method of moment (MoM) and finite-diff erence time-domain (FDTD). It is imperative to accurately assess the mutual coupling parameters in phased array antennas to ensure a thorough and precise analysis. Floquet analysis can be exploited to analyze a finite array including mutual coupling eff ects.

3- Simulation and Measured Results

In this section the simulation and measured results are investigated and explained. In order to test the antenna parameters while establishing a 90-degree phase difference, a four-port hybrid has been designed specifically for the proposed dual-port antenna [52, 53]. It is widely recognized that within the Ka frequency band, even minor alterations in physical dimensions or structures (as little as 1mm) can result in significant phase discrepancies, amounting to approximately 30 degrees. Consequently, the hybrid phase shifter has been integrated with the antenna within a multilayered antenna configuration (Figure 3). The proposed antenna and its test board, a 90-degree hybrid phase shifter, were developed and manufactured on a multilayered printed circuit board (PCB) utilizing Rogers (RO4350B) substrate.

Various Glass substrates and electrical permittivity alternatives might be utilized based on the specific application. The selected substrate for this testing is Rogers, which use epoxy/glass techniques and facilitates the manufacturing of multilayered PCBs and the technology for Blind VIAs manufacture. Rogers is used to prove the concept with readily available fabrication, and the design is directly transferable to Glass substrates. The transmission line lengths from the outputs of the hybrids to the antenna input ports are identical to minimize phase error. Figure 4 illustrates the antenna configuration integrated with hybrids/phase shifter and the multilayered double-port antenna PCB developed using Altium Designer.

The antenna underwent testing at the Anhui Engineering Research Centre for Microwave and Communications, Hefei Normal University, Hefei, China. The network analyzer utilized for assessing the scattering characteristics is the Agilent PNA-X N5247A, operating within the frequency range of 10 MHz to 67 GHz. The testing was conducted within specific frequency bandwidths and frequencies due to the hybrid's frequency band, fabrication accuracy, and frequency shift. The discrepancies noted between the simulation and the measured results can be ascribed to the inadequate isolation between the ports of the test board or hybrid phase shifter, approximately 10 dB, along with radiation from the ports and transmission lines that can further deteriorate isolation, and measurement inaccuracies related to the testing equipment, estimated to be around 2 dB, according to the specifications provided by NSI-MI Technologies and the test operator's report. Utilizing a high-precision test board or integrated circuits engineered for beamforming, capable of providing accurate phase settings and phase/amplitude adjustments, can significantly improve measurement quality, ensuring alignment with simulation outcomes and optimal performance.

Figure 5 illustrates the simulated and measured return loss and linearly polarized realized gain, simulated half power beamwidths (HPBW) and efficiencies of the antenna. The simulation results indicate that the antenna is ultra-wideband (UWB), has strong isolation between ports (>25dB), and offers a broad HPBW, as well as excellent gain and efficiency across its entire operational frequency range. The antenna's average gain is approximately 7dB and it has an ultra-wide impedance bandwidth of over 50% from 23 to 40 GHz and HPBW>80°. The low measured isolation values of the ports are the result of low isolation of hybrid phase shifter and test inaccuracies that were discussed and investigated at the paragraph three of this section. Figure 6 shows the magnetic fields or the creation of magnetic dipoles. The antenna height may be further lowered; however, this will result in a constricted operating band that shifts higher.

The antenna excites the TE_{11} fundamental mode due to the placement of feed lines along the central axes or diameters of the structure, which generates surface currents and electric fields along these lines. Figure 7 depicts the electric field vectors and surface currents, signifying the direction of polarization and the excitation of the TE_{11} mode. In addition, Figure 8 presents the active parameters of the antenna, which are derived from Floquet analysis. This illustrates the extensive scanning capabilities of the antenna when it radiates in an array. It also shows that in an array, because of mutual coupling and impedance changes, the isolations between ports decrease for wide scanning angles. Mitigation of mutual coupling can be achieved through the enhancement of shielding VIAs, the application of electromagnetic wave absorbers or metamaterials (metamaterial radomes) and/or the implementation of differential feeding techniques [54-62]. Figure 9 displays the simulated and measured circularly polarized realized gain, simulated HPBW and active realized gain. It can be inferred that the performance of the antenna within the array and in circularly-polarized mode is commendable. Figure 10 presents a comparison of the simulated and measured axial ratios as a function of frequency, accompanied by axial ratio beam patterns. The results demonstrate that the antenna displays excellent performance in circularly polarized mode. Analysis of active parameters, axial ratio beam patterns, and empirical measurements reveals that the antenna accommodates wide scanning angles ($\theta = \pm 75°$). This beneficial trait is ascribed to the existence of isolation VIAs and the compact, low-profile design of the antenna.

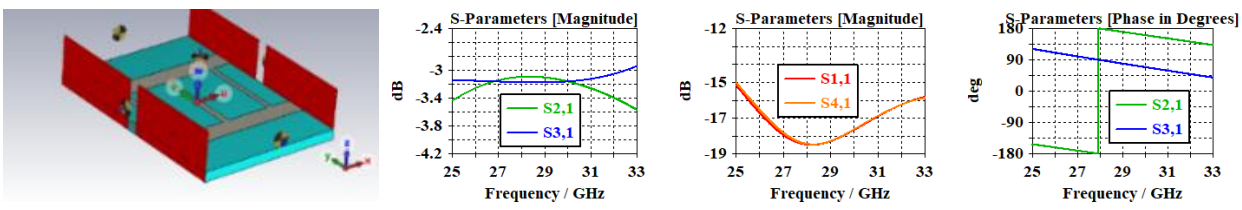

(a) (b) (c) (d)

Figure 3. Four-port 90-degree hybrid phase shifter and its specifications simulated with CST [52, 53]

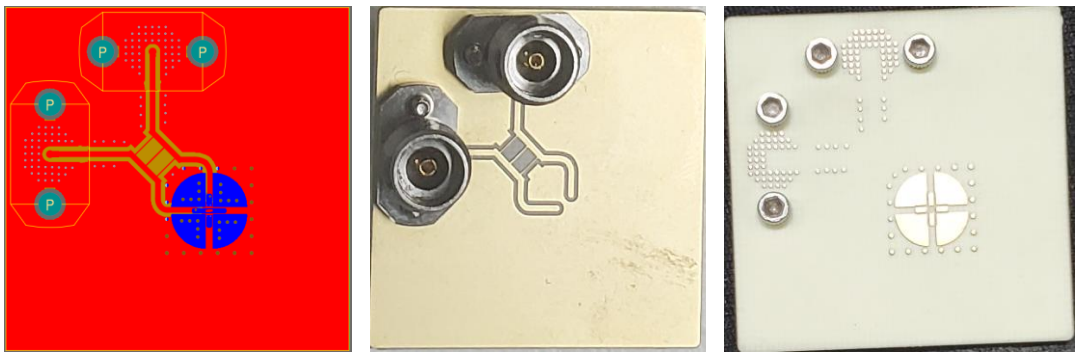

(a) (b) (c)

Figure 4. A typical designed PCB for the proposed dual-port antenna

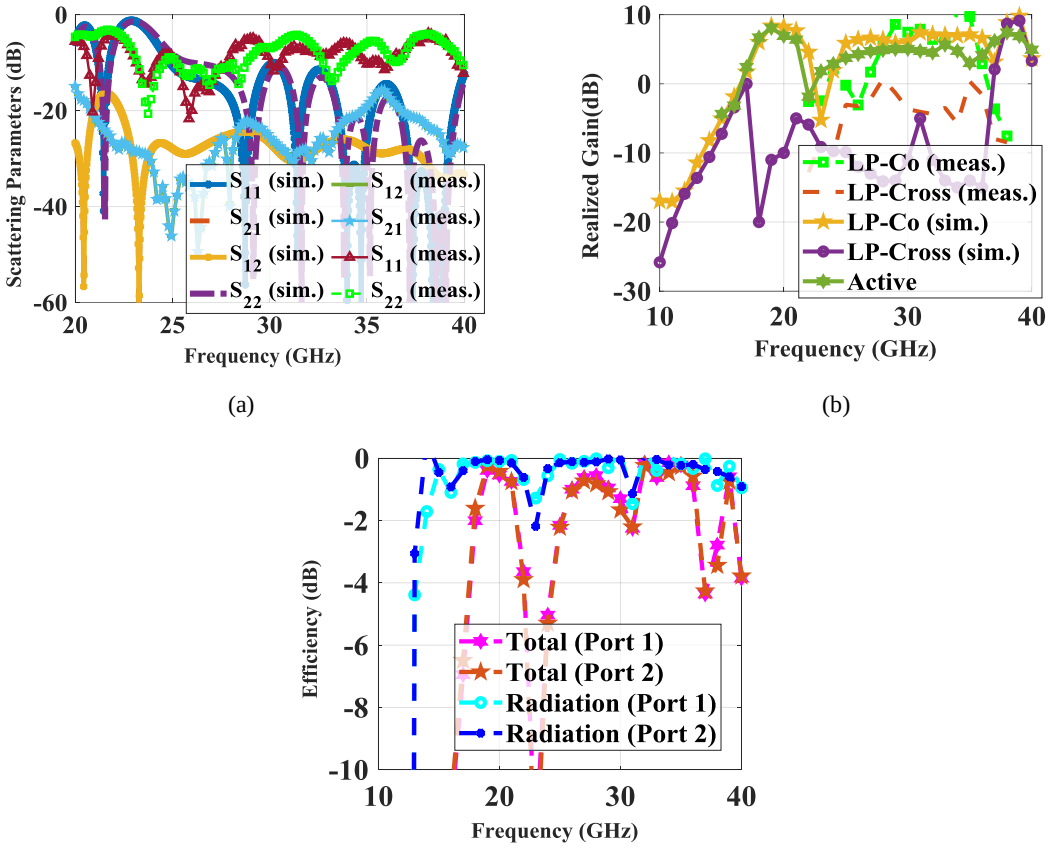

(a) (b)

(c)

Figure 5. Achieved results of the proposed antenna; a) simulated and measured return loss, b) simulated and measured linearly-polarized realized gain, c) efficiency

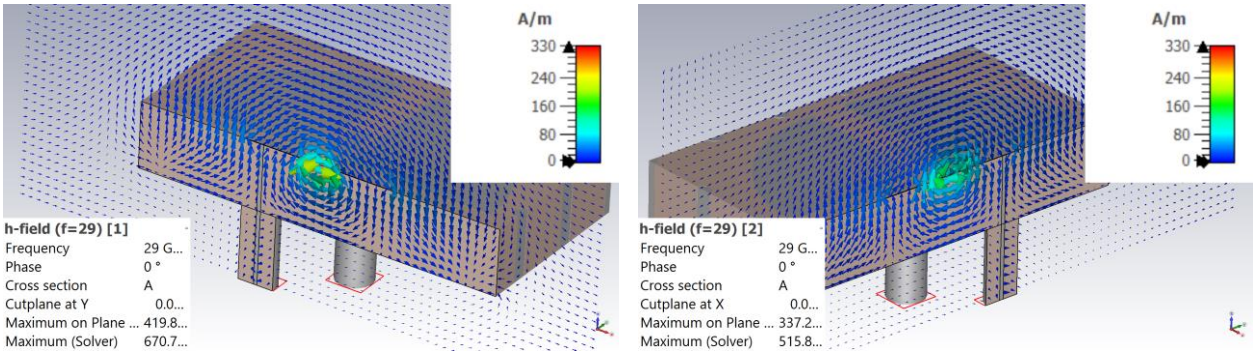

(a) (b)

Figure 6. Magnetic fields in the proposed antenna @ 29GHz for ports 1 (a) and port 2 (b)

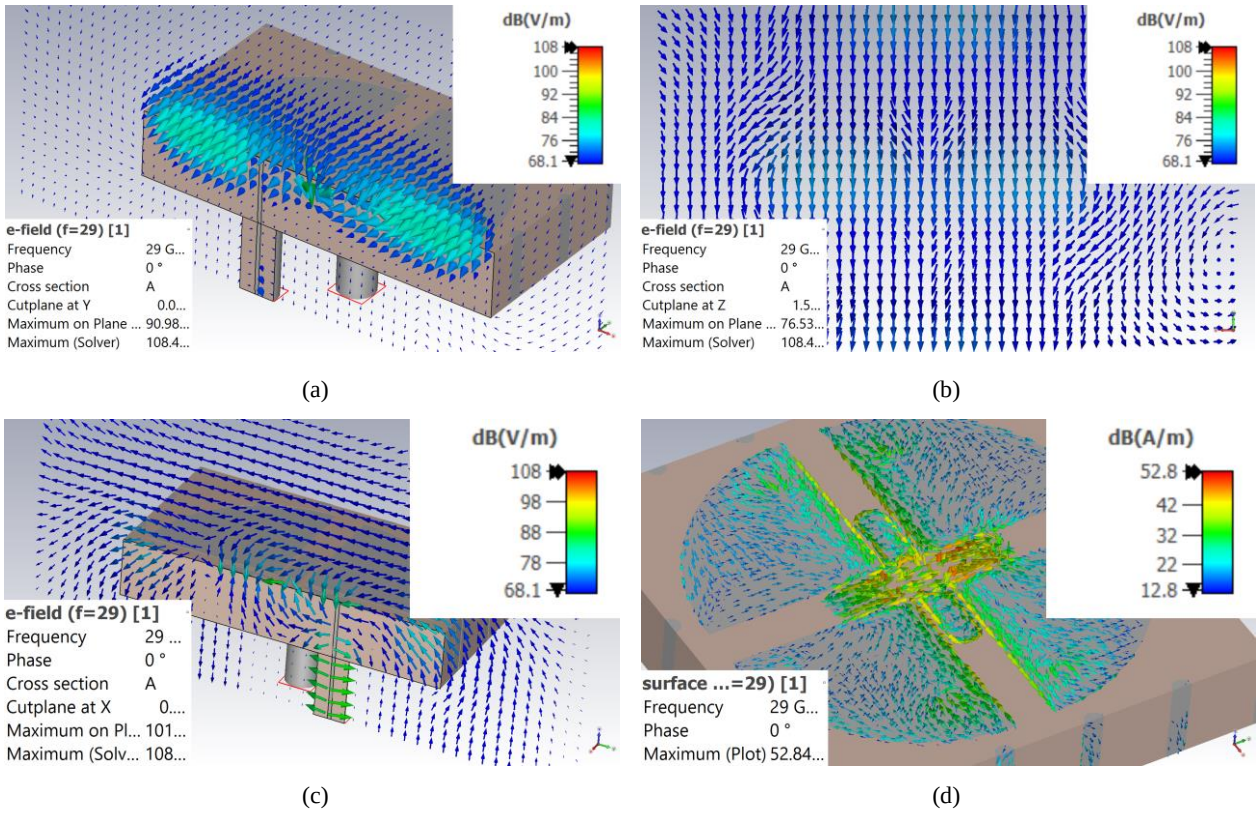

Figure 7. Electric fields in the proposed antenna at port 1 @ 29GHz; a) at XZ plane, b) at YX plane and 0.5mm above the antenna, c) electric fields in another plate, d) surface current

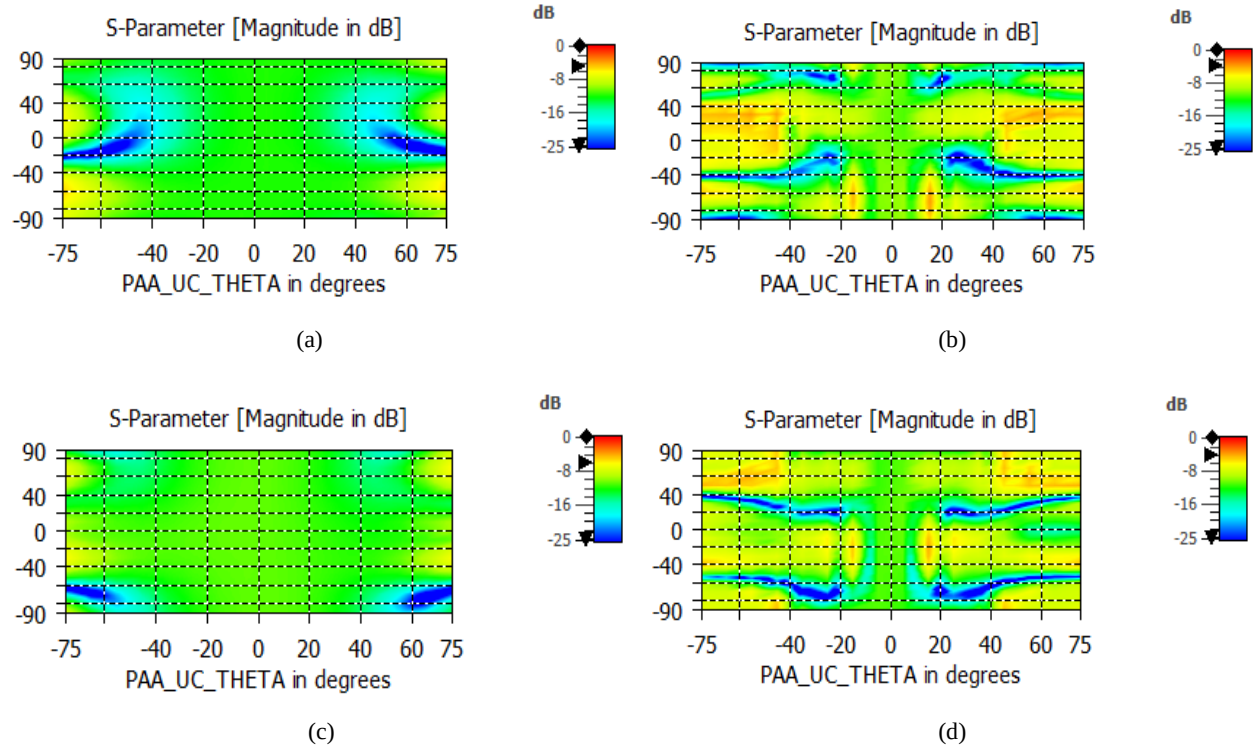

Figure 8. Active parameters of the proposed antenna as a function of scan angle; a) impedance @ 27 GHz, b) isolation @ 27 GHz, c) impedance @ 31GHz, d) isolation @ 31GHz

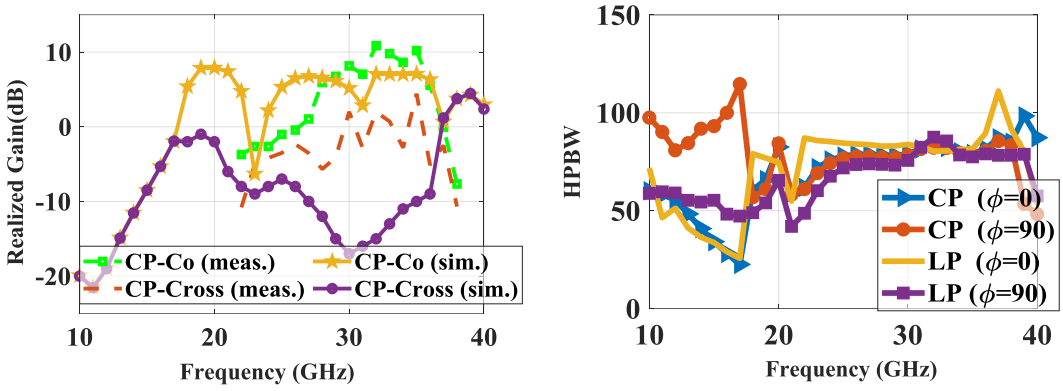

(a) (b)

Figure 9. Achieved antenna specifications; a) simulated and measured circularly-polarized realized gain, b) simulated HPBW

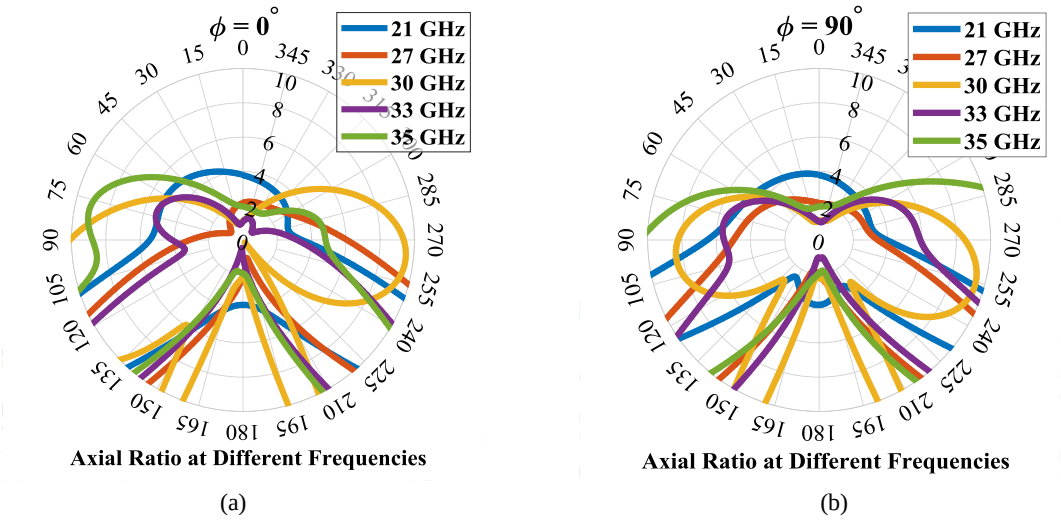

(a) (b)

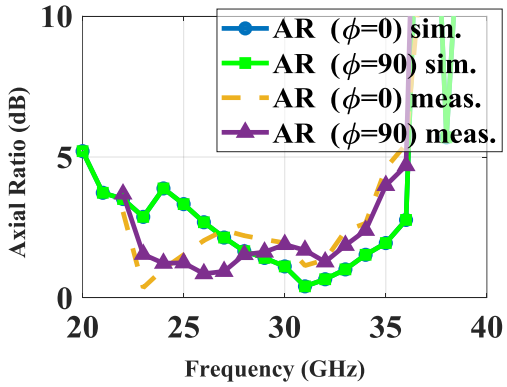

(c)

Figure 10. Achieved antenna specifications (continued); a, b) simulated axial ratio beam pattern at φ=0°, 90°, c) simulated and measured axial ratio vs. frequency

Figure 11 depicts the simulated and measured radiation patterns of the antenna in E/H- planes. The proximity of the simulated and measured values of realized gains demonstrates the antenna's high level of efficiency. At elevated frequencies (37GHz), higher-order electromagnetic waves (TM_{01}) or modes within the antenna are stimulated, enhancing radiation scanning performance as the scanning angles increase. This is due to the generation and enhancement of end-fire radiation rather than broadside radiation [63-66]. The use of gaps and/or MIM capacitors, specifically a 0.03 mm gap in VIAs linked to the radiating patches, yields a resonance frequency of 16 GHz for the patch. Adjusting this configuration produces a functional frequency range of 14 GHz to 17 GHz, so encompassing the entire frequency spectrum from 14 GHz to 40 GHz. Capacitance values ranging from 0.1 pF to 10 pF consistently influence antenna performance.

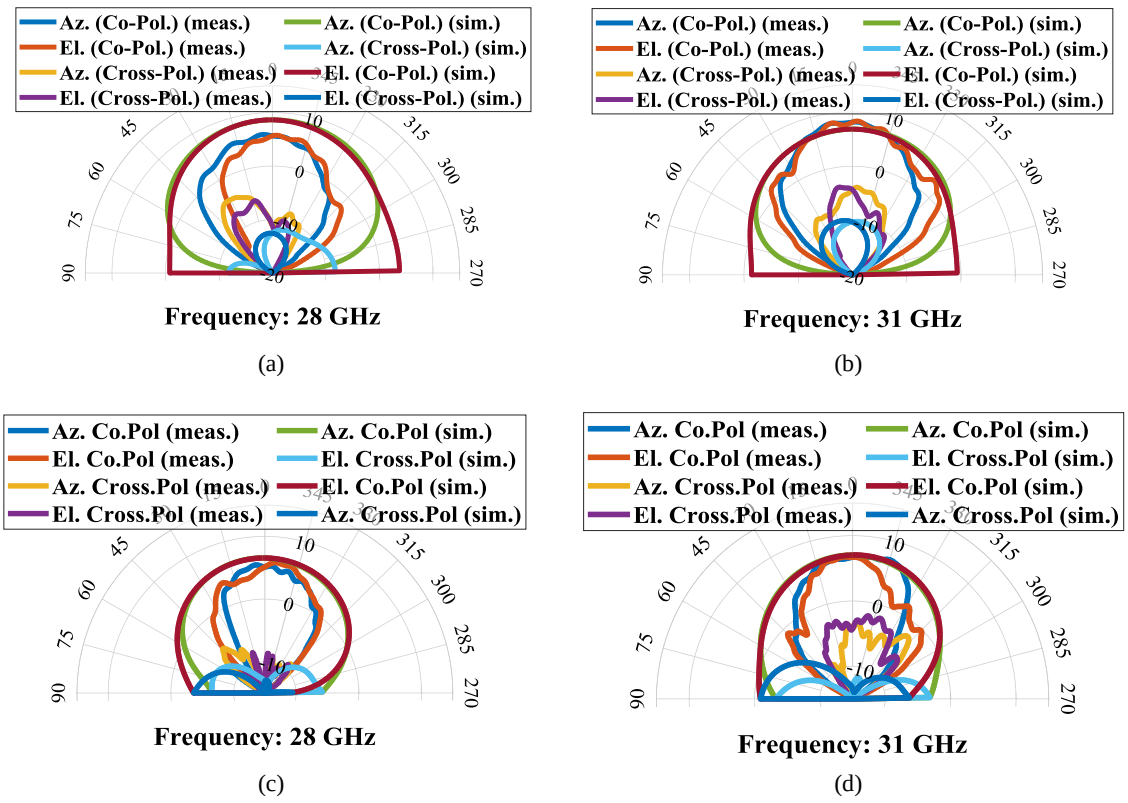

Figure 11. Simulated/measured realized gain radiation pattern; a, b) linearly polarized simulated/measured co-/cross-polarized, c, d) circularly polarized simulated/measured co-/cross-polarized

Figure 12 presents the realized gain and efficiency of the proposed adjustable MEDA. The efficiency results demonstrate that the tuning capability does not negatively affect the antenna parameters. By utilizing IC impedance transformers with appropriate impedance ratios, the performance and frequency bandwidth of the proposed antenna can be further improved. The designed antenna offers the following specifications: high gain, ultra-wideband (UWB) performance, high efficiency, wide scanning and tuning capability, and ease of fabrication using conventional PCB technologies or cost-effective standard epoxy/glass processes with only two layers. It also provides high isolation between ports and effective shielding, which prevents the formation of surface waves. Table 1 and Figure 12 further illustrate the differences and advantages of the present work compared with previously reported designs. Compared to other studies, the proposed design is dual-polarized and easy to fabricate, supports frequency tuning with a wider frequency bandwidth, exhibits broader scanning angles, and reduces the footprint by more than 30%. The thermal conductivity of the glass substrate (1.1 W/m·K) is sufficient for typical power levels. Despite the high antenna efficiency and the absence of a requirement for a cooling system, packaging options such as BGAs and thermal vias may introduce air gaps that enhance frequency bandwidth and facilitate heat dissipation and cooling for high-power applications (>10 W).

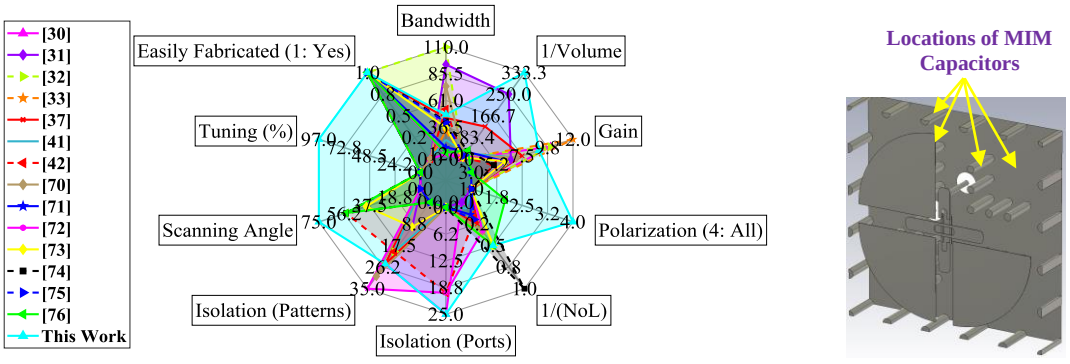

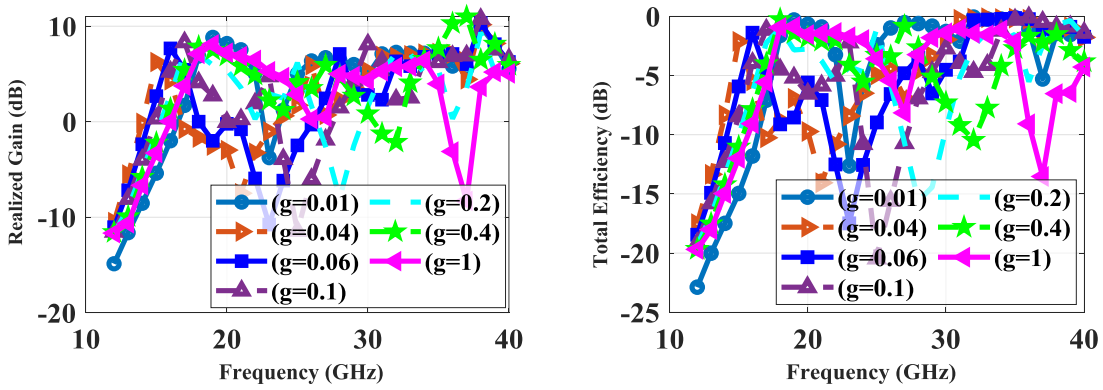

(c) (d)

Figure 12. Proposed antenna specifications; a) comparison of the proposed antenna with previous designs (refer to Table 1), b, c, d) tuning resonant frequency of the proposed antenna by MIM and/or Gap capacitors

The design parameters of the dual polarized magneto-electric antenna are (mm): thickness: h=0.6 or 1; feed offset = (-0.93, 0.06); folded dipole dimensions: (2.3×0.35); folded dipole dimensions of slots: (0.1×0.6); inner/outer curve = 0.07/0.15; second feed offset = (0.05, 1); second folded dipole dimensions: (2.34×0.35); second folded dipole dimensions of slots: (0.15×1.75); inner/outer curve = 0.07/0.15; radius of antenna/isolation VIAs: 0.26/0.18; distances of antenna/isolation VIAs: 0.55/0.47. In the figures, Az.: Azimuth (or φ =0° or E-plane); El.: Elevation (or φ =90° or H-plane); CP: Circularly-Polarized; LP: Linearly-Polarized.

4- Array Analysis

In phased array antenna, the main beam can be controlled by controlling phases of each antenna elements of the array. Also, the level of the side/minor lobes can be controlled by amplitude tapering across the array. In this section, rectangular and Sunflower array layouts are analyzed and simulated. Obtaining measurement results for rectangular and sunflower layouts requires the creation of arrays with a significant number of calibrated feeding networks and beamformer ICs. The ICs are essential for the calibration and adjustment of the antenna arrays. In addition, simulations indicate a frequency variance exceeding 0.2GHz, thereby leading to performance alterations for typical 0.01mm PCB tolerances. Thus, the discussion has solely focused on the simulation results. EM simulations in CST are based on industry-standard validation methods. Moreover, given all factors, including electromagnetic boundary conditions and modeling software, are consistent, the comparisons between the arrays are accurate.

To achieve enhanced and optimal gain in arrays, it is crucial to reduce mutual coupling by augmenting shielding VIAs and/or utilizing electromagnetic wave absorbers or metamaterials (metamaterial radomes) especially where the spacings between antenna elements are small. Coupling and surface wave attenuation can be accomplished by designing low-profile structures and/or utilizing a differential feeding mechanism [54-62]. Increased mutual coupling coefficients can diminish the overall gain of an array; however, the spacing between the antenna elements in the Sunflower array exceeds $0.5\lambda_0$, hence reducing the mutual coupling values beyond those obtained by Floquet analysis and simulations ($S_a \approx 0.75\lambda_0$). Parameters such as S_a and the minimum distance between antenna elements require tuning to get optimal gain. Notwithstanding the aforementioned issues, the studies and simulations of the arrays, employing radiation patterns produced by solvers and Floquet analyses in CST Studio Suite, demonstrate the enhanced performance and benefits of deploying the Sunflower array created with the proposed antenna elements.

In a phased array a spatial excitation taper and a progressive phase shift can also be defined for beam scanning and reducing side lobe levels (SLLs). For example, the non-uniform/Taylor excitation of layout can be implemented and used. But the non-uniform/Taylor layout or placements of the antenna elements in a Sunflower array are the same as feeding the antenna elements with Taylor distribution and without attenuation of the input/output powers of transceivers or function as array thinning in phased array antennas [67, 68]. The formulas in Figure 13, determines the placements of the antenna elements in the array to decrease side lobe and grating lobe levels in a Sunflower array layout [69]. S_a is used in the general Fermat Spiral; $S_a = F_s\sqrt{(a_g\pi)}$; where: F_s is the scaling factor of the general Fermat spiral, i.e. the radial distance of the spiral at 1 radian, and $a_g = \pi\ (3-\sqrt{5})$. In this configuration, other parameters such as the number of elements, angular displacement between elements and scaling factors can be changed.

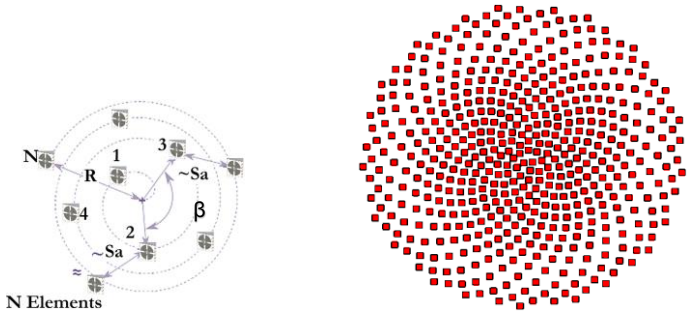

(a) (b)

Figure 13. General layout of the Fermat spiral; a) geometry ($r=S_a\times\varphi\times\sqrt{(n/p)}$; $\varphi=n\times\beta$; $\beta=\pi\times(3-\sqrt{5})$rad, b) its layout

Figure 14 shows that a Sunflower array with only N (number of antenna elements) = 512 can achieve an additional 1 dB antenna gain compared to a rectangular array employing amplitude tapering (Dolph–Chebyshev) with N = 1024 and element spacing of $d = 0.5\lambda_0$. The Sunflower layout dimensions (diameter = 175 mm) are slightly larger than those of the rectangular layout (L × W = 155 mm × 155 mm), yet it provides better specifications (Figure 15). If the element spacing in the rectangular layout is increased to $d = 0.75\lambda_0$ with N = 1024, the layout dimensions become L × W = 230 mm × 230 mm, resulting in a gain increase of 3.5 dB. To clarify, maintaining identical antenna specifications in a rectangular configuration requires the implementation of excitation tapering, an increased number of antenna elements, and/or additional spatial allocation. Furthermore, as can be observed, the cross-polarization radiation pattern values are nearly similar to those of a single antenna element when mutual coupling is negligible or can be minimized using the techniques reported in the literature.

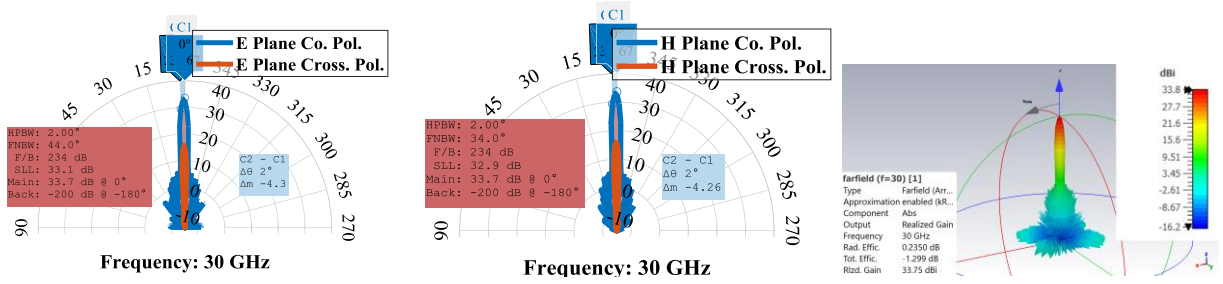

(a) (b) (c)

Figure 14. Sunflower Spiral layout radiation patterns: N=512, SLL = 30dB; a, b) 2D, c) 3D

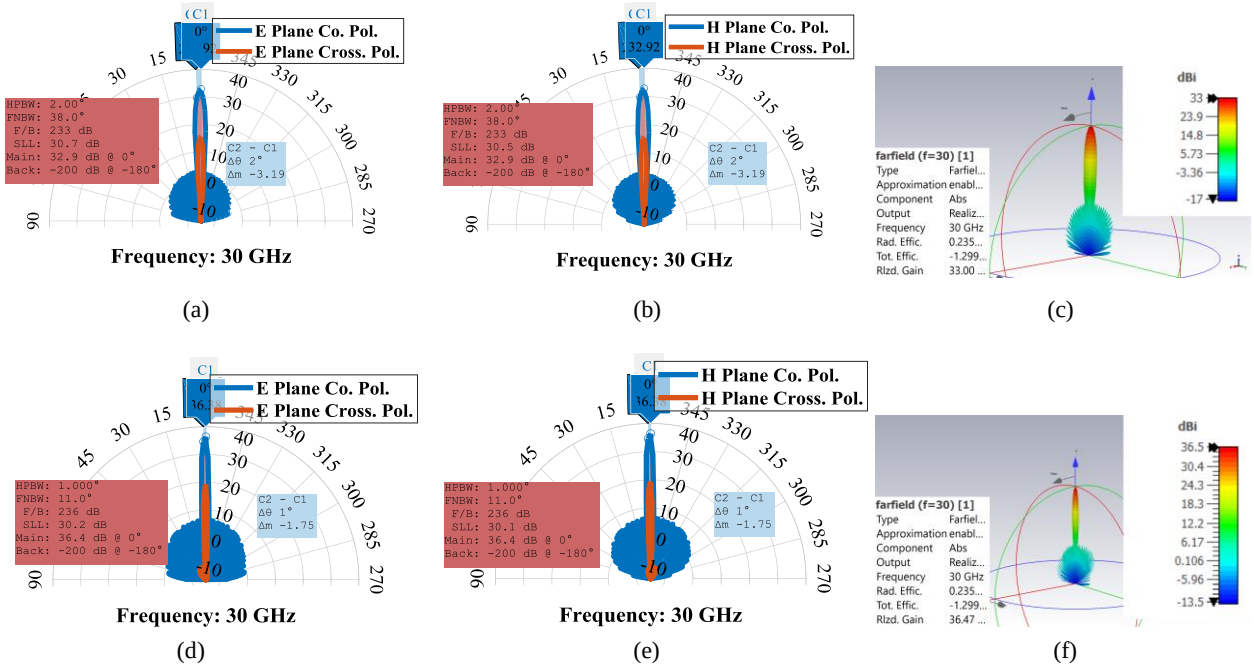

(a) (b) (c)

(d) (e) (f)

Figure 15. Square layout radiation patterns: N=1024, SLL = 30dB; a, b) 2D (d=0.5λ), c) 3D (d=0.5λ), d, e) 2D (d=0.75λ), f) 3D (d=0.75λ)

Therefore, utilizing a Sunflower layout can result in reduced sidelobe levels and an increased antenna area, or alternatively, higher array antenna gain and efficiency. The simulation results illustrate that using a Sunflower layout can provide more than 3 dB gain or at least a 50% reduction in the number of antenna elements. Employing the active radiation results of the proposed antenna element in the Sunflower array requires approximately 30% fewer antenna elements to achieve comparable array gain and specifications relative to a rectangular array. This difference is attributed to array effects and a 0.6 dB decrease in the active gain of the antenna element.

Table 1. Comparison of current work with previous med designs

Ref.	Antenna Type	Bandwidth (GHz) (%)	Element Size (λ_0)[3]	Peak Gain (dB)	Polarization/ Dual Port	Process/ Tech.[1]	Isolation Between Ports; Radiation Patterns	NoL[2]	Tunable (%)	S. A.[3]
[30]	Waveguide	24-27 (12)	3.58×6.75×1.44	10	LP/No	3D Printing	25; 25	MB[4]	No	NA
[31]	Metal	0.71-1.96 (94)	0.31×0.28×0.04	6.5	LP/No	MB	SP[5]; 10	MB	No	NA
[32]	SIW[6]	3.1-10.6 (110)	2.5×1.5×0.04	10	LP/No	PCB	SP; 20	2	No	NA
[33]	Waveguide	50-70 (33)	0.8×0.7×NA	12	LP/No	TPGW[7]	SP; 25	3	No	NA
[37]	Patch	1.7-2.7 (45)	0.46×0.3×0.06	7.5	LP/No	PCB	SP; 25	4	No	NA
[41]	Patch	22.4-29 (25.5)	0.8×0.8×0.07	7	LP/No	HDI	SP; 20	14	No	NA
[42]	Patch	25-43 (74)	0.37×0.37×1.12	5	LP/No	FOWLP	20; 20	5	No	±55°
[70]	DR[8]	2.45-5.3(74)	0.66×0.66×0.17	7	LP/No	DR+MS[9]	SP; 30	3	No	NA
[71]	Stacked	25-30 (18)	0.6×0.6×0.1	6	LP/No	PCB	NA; NA	7	No	NA
[72]	SIW	24.5-27.5 (12)	0.67×0.67×0.2	6	LP/No	PCB	20; 35	3	No	NA
[73]	LW[10] SIW	23-33 (36)	0.75×0.75×0.28	6	CP/No	PCB	0; 10	2	No	±40°
[74]	Patch	23-35 (42)	0.52×0.52×0.12	5	LP/No	PCB	SP; 20	1	No	±55°
[75]	Patch	23.5-35.5 (41)	0.57×0.57×0.24	3	LP/No	PCB	SP; 30	5	No	NA
[76]	Patch	17.7-20.2 (13)	0.5×0.5×0.12	3	CP/Yes	PCB	NA	2	No	±55°
This Work	Patch	14-17 :14-40 (97) (M. G[11]) 17-22/ 24-39 (48) 29-39 (30)	0.25×0.25×0.05 0.33×0.33×0.06/ 0.5×0.5×0.1 0.55×0.55×0.07	6 :9 8/ 9 7	Dual/Yes	Epoxy Glass/ Glass Substrate	25; 25	2	97% (M.G)	±75°

Tech.[1]: Technology; NoL[2]: Number of Dielectric Layers; S. A.[3]: Scanning Angle; MB[4]: Metal-Based; SP[5]: Single Port; SIW[6]: Substrate Integrated Waveguide; TPGW[7]: Trapped Printed Gap Waveguide; DR[8]: Dielectric; MS[9]: Microstrip; LW[10]: Leaky Wave; MG[11]: Tunable by MIM/Gap Capacitors.

5- Conclusion

This paper proposed the design, analysis, and validation of an innovative small and low-profile UWB dual-port antenna. The study employs simulations performed using CST Studio Suite software, alongside empirical measurements and the associated circuit model. The results obtained demonstrate that the antenna element exhibits high performance, characterized by superior parameters when compared to prior designs. Notably, it achieves a higher gain, a wider HPBW, and, based on the active parameters, axial ratio beam patterns, and measurements, facilitates broader scanning angles. The antenna is manufactured utilizing the specifications of glass substrates and epoxy/glass processes, allowing for easy fabrication requiring only two layers. The current design is characterized by a reduced size and thickness compared to earlier models, while also providing tuning capabilities of approximately 97% at the entire frequency range. Additionally, array and Floquet analyses have confirmed its exceptional performance in array configurations.

6- Declarations

6-1- Author Contributions

Conceptualization, A.R.D. and F.L.; methodology, A.R.D., A.M., J.W., M.N., and F.L.; software, A.R.D.; validation, A.R.D.; formal analysis, A.R.D., A.M., J.W., M.N., and F.L.; investigation, A.M., J.W., M.N., and M.D.J.; resources, F.L.; data curation, A.R.D. and F.L.; writing—original draft preparation, A.R.D.; writing—review and editing, A.R.D., A.M., J.W., M.N., and F.L.; visualization, M.D.J.; supervision, F.L. All authors have read and agreed to the published version of the manuscript.

6-2- Data Availability Statement

The data presented in this study are available in the article.

6-3- Funding

The authors received no financial support for the research, authorship, and/or publication of this article.

6-4- Acknowledgements

The first author would like to thank Prof. Z.-X. Zhang and Dr. Zhang Liang of the Anhui Normal University and Ms. Luo Qing at Multilayer PCB Technology Company (MTL) for their help and the fabrication and measurement support. The first author is especially grateful to Chinese Academy of Sciences and China Scholarship Council for their financial support for his PhD program.

6-5- Institutional Review Board Statement

Not applicable.

6-6- Informed Consent Statement

Not applicable.

6-7- Conflicts of Interest

The authors declare that there is no conflict of interest regarding the publication of this manuscript. In addition, the ethical issues, including plagiarism, informed consent, misconduct, data fabrication and/or falsification, double publication and/or submission, and redundancies have been completely observed by the authors.

7- References

[1] Kumar, S. S., Balaji, S., Devi, S. N., & Priyadharsini, V. (2024). Exploring 6G Research: Advancements, Applications, and Challenges. Development of 6G Networks and Technology, 363–377. doi:10.1002/9781394230686.ch16.

[2] Ishteyaq, I., Muzaffar, K., Shafi, N., & Alathbah, M. A. (2024). Unleashing the Power of Tomorrow: Exploration of Next Frontier With 6G Networks and Cutting Edge Technologies. IEEE Access, 12, 29445–29463. doi:10.1109/ACCESS.2024.3367976.

[3] Jiang, W., Han, B., Habibi, M. A., & Schotten, H. D. (2021). The road towards 6G: A comprehensive survey. IEEE Open Journal of the Communications Society, 2, 334–366. doi:10.1109/OJCOMS.2021.3057679.

[4] Wang, X., Mei, J., Cui, S., Wang, C. X., & Shen, X. S. (2023). Realizing 6G: The Operational Goals, Enabling Technologies of Future Networks, and Value-Oriented Intelligent Multi-Dimensional Multiple Access. IEEE Network, 37(1), 10–17. doi:10.1109/MNET.001.2200429.

[5] Quy, V. K., Chehri, A., Quy, N. M., Han, N. D., & Ban, N. T. (2023). Innovative Trends in the 6G Era: A Comprehensive Survey of Architecture, Applications, Technologies, and Challenges. IEEE Access, 11, 39824–39844. doi:10.1109/ACCESS.2023.3269297.

[6] Tyagi, A. K., Tiwari, S., Gupta, S., & Mishra, A. K. (2025). 6G - Enabled Emerging Technologies for Next- Generation Society: Challenges and Opportunities. 6G- Enabled Technologies for Next Generation, 343–406. doi:10.1002/9781394258369.ch16.

[7] Zhang, H., Yao, X., Xu, K., Wu, Z., Li, W., Lu, Y., & Yang, J. (2025). Trustworthiness Evaluation Toward 6G Support of Space-Air-Ground Integrated Network. IEEE Wireless Communications, 32(2), 34–40. doi:10.1109/MWC.001.2400273.

[8] Hazra, A., Munusamy, A., Adhikari, M., Awasthi, L. K., & Venu, P. (2024). 6G-Enabled Ultra-Reliable Low Latency Communication for Industry 5.0: Challenges and Future Directions. IEEE Communications Standards Magazine, 8(2), 36–42. doi:10.1109/MCOMSTD.0004.2300029.

[9] Mohjazi, L., Selim, B., Tatipamula, M., & Imran, M. A. (2024). The Journey toward 6G: A Digital and Societal Revolution in the Making. IEEE Internet of Things Magazine, 7(2), 119–128. doi:10.1109/IOTM.001.2300119.

[10] Hong, W., Jiang, Z. H., Yu, C., Hou, D., Wang, H., Guo, C., Hu, Y., Kuai, L., Yu, Y., Jiang, Z., Chen, Z., Chen, J., Yu, Z., Zhai, J., Zhang, N., Tian, L., Wu, F., Yang, G., Hao, Z. C., & Zhou, J. Y. (2021). The Role of Millimeter-Wave Technologies in 5G/6G Wireless Communications. IEEE Journal of Microwaves, 1(1), 101–122. doi:10.1109/JMW.2020.3035541.

[11] Maral, G., Bousquet, M., & Sun, Z. (2020). Satellite Communications Systems: Systems, Techniques and Technology, Sixth Edition. Satellite Communications Systems: Systems, Techniques and Technology, John Wiley & Sons, New Jersey, United States. doi:10.1002/9781119673811.

[12] Dastkhosh, A. R., Khan, Z., Naseh, M., & Lin, F. (2022). Link Budget Calculations for K/Ka-band Satellite Mobile Communication Systems. 2022 IEEE MTT-S International Wireless Symposium, IWS 2022 - Proceedings, 1–3. doi:10.1109/IWS55252.2022.9978012.

[13] Ippolito, L. J. (2008). Satellite Communications Systems Engineering: Atmospheric Effects, Satellite Link Design and System Performance. Wiley, West Sussex, United Kingdom. doi:10.1002/9780470754443.

[14] Dastkhosh, A. R., Naseh, M., Dardari, D., & Lin, F. (2022). TV-Based Phased Array System Design in BTSs for 5G/IoT Applications. Progress in Electromagnetics Research C, 127, 1–16. doi:10.2528/PIERC22091909.

[15] Low, K. K. W., Zihir, S., Kanar, T., & Rebeiz, G. M. (2022). A 27-31-GHz 1024-Element Ka-Band SATCOM Phased-Array Transmitter with 49.5-dBW Peak EIRP, 1-dB AR, and ±70° Beam Scanning. IEEE Transactions on Microwave Theory and Techniques, 70(3), 1757–1768. doi:10.1109/TMTT.2021.3139911.

[16] Ur Rehman, M., Ravichandran, S., Watanabe, A. O., Erdogan, S., & Swaminathan, M. (2021). Characterization of ABF/Glass/ABF Substrates for mmWave Applications. IEEE Transactions on Components, Packaging and Manufacturing Technology, 11(3), 384–394. doi:10.1109/TCPMT.2021.3061485.

[17] Yu, T., & Yu, D. (2023). Electrical performance characterization of glass substrate for millimeter-wave applications. Journal of Materials Science: Materials in Electronics, 34(2), 126. doi:10.1007/s10854-022-09583-x.

[18] Wang, Y., & Qu, S. W. (2023). Dual-Polarized Conformal Transparent Antenna Array with Hemispherical Beam Coverage. IEEE Antennas and Wireless Propagation Letters, 22(10), 2452–2456. doi:10.1109/LAWP.2023.3291013.

[19] Dastkhosh, A. R., & Lin, F. (2023). Differential Dual Polarized Magneto-Electric Dipoles for SATCOM Applications. 2023 IEEE 11th Asia-Pacific Conference on Antennas and Propagation, APCAP 2023 - Proceedings, 1–2. doi:10.1109/APCAP59480.2023.10470287.

[20] ASE. (2025). Antenna in Package (AiP). ASE Technology Holding Co., Ltd., Kaohsiung, Taiwan. Available online: https://ase.aseglobal.com/en/technology/antenna_in_package (accessed on November 2025).

[21] Insight SiP. (2025). Index of /fichiers_insightsip. Insight SiP, Sophia Antipolis, France. Available online: https://www.insightsip.com/fichiers_insightsip (accessed on November 2025).

[22] Liu, D., Gu, X., Baks, C. W., & Valdes-Garcia, A. (2017). Antenna-in-Package Design Considerations for Ka-Band 5G Communication Applications. IEEE Transactions on Antennas and Propagation, 65(12), 6372-6379. doi:10.1109/TAP.2017.2722873.

[23] Liu, D., & Zhang, Y. (2020). Antenna-in-package Technology and Applications. John Wiley & Sons, New Jersey, United States.

[24] Chaloun, T., Brandl, S., Ambrosius, N., Krohnert, K., Maune, H., & Waldschmidt, C. (2023). RF Glass Technology Is Going Mainstream: Review and Future Applications. IEEE Journal of Microwaves, 3(2), 783–799. doi:10.1109/JMW.2023.3256413.

[25] Balanis, C. A. (2016). Antenna Theory: Analysis and Design. John Wiley & Sons, New Jersey, United States.

[26] Ding, C. F., Zhang, X. Y., Zhang, Y., Pan, Y. M., & Xue, Q. (2018). Compact broadband dual-polarized filtering dipole antenna with high selectivity for base-station applications. IEEE Transactions on Antennas and Propagation, 66(11), 5747–5756. doi:10.1109/TAP.2018.2862465.

[27] Xu, Y., Zhou, M., Wang, A., & Hou, J. (2023). Design of a compact magneto-electric dipole antenna. Microwave and Optical Technology Letters, 65(8), 2331–2336. doi:10.1002/mop.33683.

[28] Ge, L., & Luk, K. M. (2012). A Low-Profile Magneto-Electric Dipole Antenna. IEEE Transactions on Antennas and Propagation, 60(4), 1684–1689. doi:10.1109/TAP.2012.2186260.

[29] Li, M., & Luk, K. M. (2015). Wideband magnetoelectric dipole antennas with dual polarization and circular polarization. IEEE Antennas and Propagation Magazine, 57(1), 110–119. doi:10.1109/MAP.2015.2397091.

[30] Wang, H., Bae Park, Y., & Park, I. (2025). Low-Profile Magneto-Electric Dipole Antenna with Capacitively Loaded Loop and Stub-Added Notch. IEEE Transactions on Antennas and Propagation, 73(8), 6163–6168. doi:10.1109/TAP.2025.3564485.

[31] He, W., Li, J., Wu, S., Yan, S., & Xu, K. Da. (2025). 3D printed millimeter-wave magnetoelectric dipole antenna array fed by filtering butler matrix. AEU - International Journal of Electronics and Communications, 191, 155664. doi:10.1016/j.aeue.2025.155664.

[32] Kang, K., Shi, Y., & Liang, C. H. (2017). Substrate Integrated Magneto-Electric Dipole for UWB Application. IEEE Antennas and Wireless Propagation Letters, 16, 948–951. doi:10.1109/LAWP.2016.2615046.

[33] Hamada, H., Ali, M. M. M., Shams, S. I., Khalaf, A. A. M., & Allam, A. M. M. A. (2025). Design and analysis of a 60 GHz high gain wideband magneto electric dipole antenna array based on trapped printed gap waveguide technology. Scientific Reports, 15(1), 23649. doi:10.1038/s41598-025-08589-9.

[34] Wang, D. S., Zhao, P., & Chan, C. H. (2016). Design and Analysis of a High-Selectivity Frequency-Selective Surface at 60 GHz. IEEE Transactions on Microwave Theory and Techniques, 64(6), 1694–1703. doi:10.1109/TMTT.2016.2557325.

[35] Luk, K. M., & Wong, H. (2006). A New Wideband Unidirectional Antenna Element. International Journal of Microwave and Optical Technology, 1(1), 35–44.

[36] Nagarnaik, S., & Mukherjee, J. (2023). Wideband low-profile magneto–electric dipole antenna stacked with patch and metasurface. Electronics Letters, 59(17), e12934. doi:10.1049/ell2.12934.

[37] Chen, Y., Zeng, F. chao, & Zhang, Z. Y. (2025). A Low-Profile Folded Magnetoelectric Dipole Antenna for Mobile Communication. IEEE Antennas and Wireless Propagation Letters, 24(5), 1139–1143. doi:10.1109/LAWP.2025.3527565.

[38] Tian, Y. Z., Pan, Y. M., Liu, X. Y., & Leung, K. W. (2023). An SIW-based wideband endfire filtering magneto-electric dipole antenna for millimeter-wave applications. IEEE Transactions on Antennas and Propagation, 71(12), 9986-9991. doi:10.1109/TAP.2023.3328113.

[39] Yang, Y. H., Liu, B. Y., & Zhou, S. G. (2023). A Wideband Cavity-Backed Dual-Polarized Antenna for X-Band Applications. IEEE Antennas and Wireless Propagation Letters, 22(4), 913–917. doi:10.1109/LAWP.2022.3228119.

[40] Yang, S. J., Pan, Y. M., Zhang, Y., Gao, Y., & Zhang, X. Y. (2019). Low-Profile Dual-Polarized Filtering Magneto-Electric Dipole Antenna for 5G Applications. IEEE Transactions on Antennas and Propagation, 67(10), 6232–6243. doi:10.1109/TAP.2019.2925151.

[41] Qian, Z., Huang, Y., Wang, B., Qin, Q., Ge, L., & Mao, J. (2025). A Low-Profile Filtering Magneto-Electric Dipole Antenna Based on High-Density-Interconnect (HDI) Packaging. IEEE Transactions on Components, Packaging and Manufacturing Technology, 15(1), 206–213. doi:10.1109/TCPMT.2024.3507083.

[42] Yu, B., Qian, Z., Lin, C., Lin, J., Zhang, Y., Yang, G., & Luo, Y. (2021). A wideband MMWAVE antenna in fan-out wafer level packaging with tall vertical interconnects for 5g wireless communication. IEEE Transactions on Antennas and Propagation, 69(10), 6906–6911. doi:10.1109/TAP.2021.3087859.

[43] Swaminathan, M., Li, X., Vijay Kumar, L. N., Jia, X., Erdogan, S., Rehman, M. Ur, Huang, K. Q., Kim, J. W., Al-Juwhari, M., & Ahamed, M. (2025). Glass Packaging for 6G Applications. IEEE Microwave Magazine, 26(6), 46–64. doi:10.1109/MMM.2025.3540325.

[44] Dong, H. J., Kim, Y. B., Joung, J., & Lee, H. L. (2020). High gain and low-profile stacked magneto-electric dipole antenna for phased array beamforming. IEEE Access, 8, 180295-180304. doi:10.1109/ACCESS.2020.3027813.

[45] Chen, Z. N., Liu, D., Nakano, H., Qing, X., & Zwick, T. (2016). Handbook of antenna technologies. In Handbook of Antenna Technologies. Springer Publishing Company, Singapore. doi:10.1007/978-981-4560-44-3.

[46] Sosa, G. H. (2011). Electrical modeling and optimization of multilayer via transitions for fully-integrated systems. Doctoral dissertation, Doktora Tezi, National Institute for Astrophysics, Optics and Electronics (INAOE), Elektronik Bölümü, Tonantzintla, Puebla, México.

[47] Hong, J. S. (2011). Microstrip Filters for RF/Microwave Applications, Second Edition. In Microstrip Filters for RF/Microwave Applications. Wiley, New York, United States. doi:10.1002/9780470937297.

[48] Baena, J. D., Bonache, J., Martín, F., Sillero, R. M., Falcone, F., Lopetegi, T., Laso, M. A. G., García-García, J., Gil, I., Portillo, M. F., & Sorolla, M. (2005). Equivalent-circuit models for split-ring resonators and complementary split-ring resonators coupled to planar transmission lines. IEEE Transactions on Microwave Theory and Techniques, 53(4-II), 1451–1460. doi:10.1109/TMTT.2005.845211.

[49] Komanduri, V. R., Jackson, D. R., Williams, J. T., & Mehrotra, A. R. (2013). A general method for designing reduced surface wave microstrip antennas. IEEE Transactions on Antennas and Propagation, 61(6), 2887–2894. doi:10.1109/TAP.2013.2254441.

[50] Fang, Y., & Zhang, Y. P. (2021). On Surface-Wave Suppression of Differential Circular Microstrip Antennas. IEEE Antennas and Wireless Propagation Letters, 20(9), 1691–1695. doi:10.1109/LAWP.2021.3093763.

[51] Bhattacharyya, A. K. (2006). Phased array antennas: Floquet analysis synthesis. BFNs and Active Array Systems. Wiley, New York, United States.

[52] Yoon, H. J., & Min, B. W. (2017). Two section wideband 90° hybrid coupler using parallel-coupled three-line. IEEE Microwave and Wireless Components Letters, 27(6), 548–550. doi:10.1109/LMWC.2017.2701304.

[53] Chiu, L. (2014). Wideband microstrip 90 hybrid coupler using high pass network. International Journal of Microwave Science and Technology, 2014(1), 854346. doi:10.1155/2014/854346.

[54] Choi, J. R., Cheon, S. J., Lee, H. J., Lee, S. Bok, Park, B., & Lee, H. (2025). Ultra-wideband electromagnetic wave absorption in mmWave using dual-loss engineered M-type hexaferrite: A wave cancellation approach. Materials and Design, 255, 114220. doi:10.1016/j.matdes.2025.114220.

[55] Govindarajan, G., Mohammed, G. N. A., Savarimuthu, K., & Veeraselvam, A. (2023). Miniaturized electromagnetic absorber for millimeter-wave RADAR systems. Applied Physics A: Materials Science and Processing, 129(8), 557. doi:10.1007/s00339-023-06857-x.

[56] Xi, B., Xiao, Y., Li, M., Li, Y., Sun, H., & Chen, Z. (2021). Wide-Angle Scanning Phased Array Antennas Using Metasurface Slabs. IEEE Transactions on Antennas and Propagation, 69(12), 9003–9008. doi:10.1109/TAP.2021.3098569.

[57] Zhang, Y. (2024). Differential Antennas: Theory and Practice. John Wiley & Sons, Inc., New Jersey, United States.

[58] Li, Q., Peng, L., Zhang, X., Tang, J., Pang, X., Zhao, S., Xu, K., & Ye, D. (2025). Wide-Angle Surface Wave Reduction Based on Spatial Kramers–Kronig Media. IEEE Transactions on Antennas and Propagation, 73(8), 5658–5666. doi:10.1109/TAP.2025.3567468.

[59] Ramos, A., Varum, T., & Matos, J. N. (2023). A Review on Mutual Coupling Reduction Techniques in mmWaves Structures and Massive MIMO Arrays. IEEE Access, 11, 143143–143166. doi:10.1109/ACCESS.2023.3343107.

[60] Narayanaswamy, N. K., Satheesha, T. Y., Alzahrani, Y., Pandey, A., Dwivedi, A. K., Singh, V., & Tolani, M. (2024). Metasurface absorber for millimeter waves: a deep learning-optimized approach for enhancing the isolation of wideband dual-port MIMO antennas. Scientific Reports, 14(1), 30199. doi:10.1038/s41598-024-81854-5.

[61] Usman Raza, M., Zhang, K., & Yan, S. (2024). Metasurface-Assisted mutual coupling suppression in circularly polarized MIMO antenna array for Sub-6 GHz applications. Materials and Design, 248, 113445. doi:10.1016/j.matdes.2024.113445.

[62] Zhang, J., Zhang, S., Dong, J., Wang, M., Luo, H., Wu, R., & Xiao, C. (2025). Design of an ultra-wideband flexible optically transparent metamaterial absorber with wide-angle and polarization stability. Materials and Design, 253, 113921. doi:10.1016/j.matdes.2025.113921.

[63] Zhou, H., Geng, J., & Jin, R. (2022). A Magnetic Yagi-Uda Antenna with Vertically Polarized Endfire Radiation in Millimeter-Wave Band Applying Higher Order Mode. IEEE Transactions on Antennas and Propagation, 70(10), 8941–8950. doi:10.1109/TAP.2022.3177476.

[64] Song, Y., Luo, Y., Yan, N., Hou, Y., An, W., & Ma, K. (2025). Compact and Gain-Enhanced Directive Endfire Higher-Order-Mode Meander Dipole via Asymmetrically Loading Stubs. IEEE Transactions on Antennas and Propagation, 73(2), 706–714. doi:10.1109/TAP.2024.3474185.

[65] Guha, D., Banerjee, A., Kumar, C., & Antar, Y. M. M. (2012). Higher order mode excitation for high-gain broadside radiation from cylindrical dielectric resonator antennas. IEEE Transactions on Antennas and Propagation, 60(1), 71–77. doi:10.1109/TAP.2011.2167922.

[66] Sun, L., Li, Y., & Zhang, Z. (2022). Wideband Dual-Polarized Endfire Antenna Based on Compact Open-Ended Cavity for 5G Mm-Wave Mobile Phones. IEEE Transactions on Antennas and Propagation, 70(3), 1632–1642. doi:10.1109/TAP.2021.3113701.

[67] Haupt, R. L. (2015). Adaptively thinned arrays. IEEE Transactions on Antennas and Propagation, 63(4), 1626–1632. doi:10.1109/TAP.2015.2394785.

[68] Merrill, S., & Skolnik, E. (2008). Radar Handbook. McGraw Hill, New York, United States.

[69] Vigano, M. C. (2011). Sunflower array antenna for multi-beam satellite applications. TU Delft Repository, Delft, Netherland. Available online: https://repository.tudelft.nl/islandora/object/uuid%3A33e95433-514f-4367-8385-ae3cc9ddc6f5 (accessed on November 2025).

[70] Song, C., Bennett, E. L., Xiao, J., & Huang, Y. (2021). Multimode Hybrid Antennas Using Liquid Dielectric Resonator and Magneto-Electric Dipole. IEEE Transactions on Antennas and Propagation, 69(6), 3132–3143. doi:10.1109/TAP.2020.3037765.

[71] Du, J. K., So, K., Ra, Y., Jung, S. Y., Kim, J., Kim, S. Y., Woo, S., Kim, H. T., Ho, Y. C., & Paik, W. (2017). Dual-polarized patch array antenna package for 5G communication systems. 2017 11th European Conference on Antennas and Propagation, EUCAP 2017, 3493–3496. doi:10.23919/EuCAP.2017.7928848.

[72] Feng, B., Chen, J., Chung, K. L., Wang, L., & Li, Y. (2022). Dual-polarized Filtering Magneto-Electric Dipole Antenna Arrays with High Radiation-Suppression Index for 5G New Radio n258 Operations. IEEE Transactions on Antennas and Propagation, 70(4), 3058–3063. doi:10.1109/TAP.2021.3121095.

[73] Yang, X. X., Qiu, H., Lou, T., Yi, Z., Cao, Q. D., & Gao, S. (2022). Circularly Polarized Millimeter Wave Frequency Beam Scanning Antenna Based on Aperture-Coupled Magneto-Electric Dipole. IEEE Transactions on Antennas and Propagation, 70(9), 7603–7611. doi:10.1109/TAP.2022.3191983.

[74] Zhao, L., Li, Y., Wang, J., & Ge, L. (2023). A Study on Millimeter-Wave Magneto-Electric Dipole Phased Arrays for 5G Dual-Band Applications. IEEE Transactions on Antennas and Propagation, 71(3), 2375–2384. doi:10.1109/TAP.2022.3209173.

[75] Li, Y., Jian, P., Xi, D., Wu, F., Jiang, Z. H., & Hong, W. (2024). A Wideband Transmitarray Antenna Based on True-Time Delay Magneto-Electric Dipole Elements. IEEE Transactions on Circuits and Systems II: Express Briefs, 71(7), 3353–3357. doi:10.1109/TCSII.2024.3366658.

[76] Zhao, D., Gu, P., Yi, Y., Zhang, J., Xu, C., Yang, M., Chen, Z., Chai, Y., Liu, H., Jiang, S., Yan, X., & You, X. (2023). A K-Band Hybrid-Packaged Temperature-Compensated Phased-Array Receiver and Integrated Antenna Array. IEEE Transactions on Microwave Theory and Techniques, 71(1), 409–423. doi:10.1109/TMTT.2022.3225289.